View metadata, citation and similar papers at core.ac.uk
brought to you by CORE
provided by Scipedia

# A time-dependent anisotropic model for argillaceous rocks. Application to an underground excavation in Callovo-Oxfordian claystone.

**Miguel Mánica** (miguel.angel.manica@estudiant.upc.edu)
Department of Civil and Environmental Engineering
Universitat Politècnica de Catalunya, Barcelona Tech, Spain

**Antonio Gens** (antonio.gens@upc.edu)
Department of Civil and Environmental Engineering
Universitat Politècnica de Catalunya, Barcelona Tech, Spain

**Jean Vaunat** (jean.vaunat@upc.edu)
Department of Civil and Environmental Engineering
Universitat Politècnica de Catalunya, Barcelona Tech, Spain

**Daniel F. Ruiz** (daniel.ruiz.restrepo@gmail.com)
Department of Civil and Environmental Engineering
Universitat Politècnica de Catalunya, Barcelona Tech, Spain

## Abstract

The paper presents a constitutive model for argillaceous rocks, developed within the framework of elastoplasticity, that includes a number of features that are relevant for a satisfactory description of their hydromechanical behaviour: anisotropy of strength and stiffness, behaviour nonlinearity and occurrence of plastic strains prior to peak strength, significant softening after peak, time-dependent creep deformations and permeability increase due to damage. Both saturated and unsaturated conditions are envisaged. The constitutive model is then applied to the simulation of triaxial and creep tests on Callovo-Oxfordian (COx) claystone. Although the main objective has been the simulation of the COx claystone behaviour, the model can be readily used for other argillaceous materials. The constitutive model developed is then applied, via a suitable coupled hydromechanical formulation, to the analysis of the excavation of a drift in the Meuse/Haute-Marne

Underground Research Laboratory. The pattern of observed pore water pressures and displacements, as well as the shape and extent of the damaged zone, are generally satisfactorily reproduced. The relevance and importance of rock anisotropy and of the development of a damaged zone around the excavations are clearly demonstrated.

**Keywords**: Argillaceous rocks, anisotropy, time-dependent behaviour, elasto-plasticity, coupled hydromechanical analysis, tunnel excavation.

## 1. Introduction

Argillaceous rocks and stiff clay formations have great potential as possible geological host medium for radioactive waste. These materials have low permeability, significant retardation properties for radionuclide migration, no economic value (with the exception of gas or oil shales) and they often exhibit a significant capacity of hydraulic self-sealing of fractures [1,2]. Therefore, a proper understanding and an appropriate modelling of their hydromechanical behaviour are of immediate interest. Although there are notable differences between different argillaceous formations [3,4], reflecting their various origins and geological histories, there are also a number of common key features (e.g. time-dependent behaviour, anisotropy, some degree of softening, variation of permeability with damage) [3,5-7] that should be considered in any description of their behaviour.

There have already been quite a number of proposals of constitutive laws that incorporate one or more of those features listed above. From a macroscopic point of view models based on plasticity [8-14] or coupled damage-plasticity [15] have been widely employed. Also, combined micro- and macro-mechanical approaches have been recently applied via homogenization techniques [16,17]. All of these models are capable of

reproducing a post peak brittle behaviour and some of them also incorporate other features like time dependency [14,17]

The work presented in this paper has been developed in the context of the activities being carried out in the Meuse/Haute-Marne (MHM) Underground Research Laboratory (URL), located in Eastern France near the town of Bure**,** constructed and operated by the French national radioactive waste management agency (ANDRA). It consists of two shafts (an access shaft and a ventilation shaft) and a network of drifts, excavated at a depth of 490 m, in which several *in situ* experiments have been performed [18]. The facility is excavated in Callovo-Oxfordian (COx) claystone, an argillaceous rock that has been intensively studied in recent years [19 this issue]; some reference properties are shown in Table 1. Laboratory studies have revealed, among others, the following features of behaviour:

- Anisotropy of strength and stiffness in the directions parallel and orthogonal to the bedding planes;
- Significant stress-strain nonlinearity and plastic strains prior to peak strength, with a yield limit identified at about 50% of the maximum deviatoric stress;
- A quasi-brittle behaviour at the in situ stress range, with a significant strength loss after the peak deviatoric stress;
- Creep deformations with increasing strain rates for higher deviatoric stresses.

In this paper, a constitutive model is described aimed to reproduce the main features of behaviour of the COx claystone as listed above. Specifically, it incorporates strength and stiffness anisotropy, nonlinear isotropic hardening to account for plastic deformations prior peak strength, softening behaviour after peak, a non-associated flow rule, time-dependent deformations and dependency of permeability on irreversible strains. Although the main

objective has been the simulation of the behaviour of the COx claystone, the model can be readily applied to other argillaceous materials since they usually exhibit, as pointed out above, similar features of behaviour.

The constitutive law developed has then been applied to the simulation of an underground excavation in the MHM URL. The work has been developed in the context of the "Transverse Action" benchmark programme [20 this issue]. Although all the calculations requested have been performed, for space reasons only the analysis corresponding to the hydromechanical modelling excavation of the GCS drift are reported here as it is the more fully instrumented case. Also, the GCS drift is aligned with the major horizontal principal stress resulting in a nearly isotropic stress state in the cross-section perpendicular to the axis of the opening. Thus, in this case, the effects of material anisotropy can be readily identified.

## 2. Hydromechanical constitutive model

Both saturated and unsaturated conditions have been considered in the development of the model. As shown later, consideration of unsaturated condition provides a more realistic setting for modelling laboratory tests. Also, potential desaturation of the rock during excavation can then be readily accommodated in the analysis, if necessary. To this end, a generalized effective stress expression has been adopted:

$$\boldsymbol{\sigma}' = \boldsymbol{\sigma} + S_e s\, B\, \mathbf{I} \tag{1}$$

where $\boldsymbol{\sigma}'$ is the effective stress tensor, $\boldsymbol{\sigma}$ is the total stress tensor, $S_e$ is the equivalent degree of saturation (defined below), $s$ is suction, $B$ is Biot's coefficient and $\mathbf{I}$ is the identity tensor.

Naturally, for saturated conditions, equation (1) reduces to:

$$\boldsymbol{\sigma}' = \boldsymbol{\sigma} - p_l \; B \; \mathbf{I} \tag{2}$$

where liquid (water) pressure, $p_l$, is equated to $-s$.

From a number of experimental and *in situ* observations of COx claystone, two main deformation mechanisms can be identified: an instantaneous mechanism related to the immediate deformation due to changes in effective stress and a purely time-dependent response occurring under constant effective stress. Note that, the instantaneous response also includes the deformation caused by changes of effective stress associated with consolidation processes (i.e. hydromechanical coupling).

*2.1 Instantaneous mechanism*

The instnataneous response is described within the framework of elasto-plasticity because it provides a flexible platform to introduce the model features required to simulate the behaviour of argillaceous rock. Inside the yield surface, the response is assumed cross-anisotropic elastic, with a vertical symmetry axis. In this context, it is important to point out that when the term “damage”, is used in this paper, it refers to a state of the material and not to the concept associated with damage mechanics theory (e.g. [21]).

At higher deviatoric stresses, plastic deformations develop. On reaching the yield surface, plastic strains accumulate that are physically related to the development and growth of microcracks and they are modelled by hardening plasticity. Therefore, further loads can be sustained by the material until reaching the failure surface that represents the maximum strength of the material. From that point onwards, strength is gradually reduced to its residual value. This is related to the coalescence of microcracks into macrocraks and

it is modelled through softening plasticity. The Mohr-Coulomb criterion is used for both yield and failure limits. In terms of stress invariants, this criterion is expressed by Eq. (3), which produces a cone in the principal stress space, with a hexagonal cross section in the deviatoric plane. Corners have been smoothed using Sloan & Booker [22] procedure.

$$f = \left( \cos\theta + \frac{1}{\sqrt{3}} \sin\theta \sin\varphi \right) J - \sin\varphi \left( c \cot\varphi + p' \right) = 0 \tag{3}$$

where $\varphi$ is the friction angle, $c$ is the cohesion and the remaining variables are stress invariants given by the following expressions,

$$p' = \frac{1}{3} \left( \sigma'_{xx} + \sigma'_{yy} + \sigma'_{zz} \right) \tag{4a}$$

$$J = \left( \frac{1}{2} \operatorname{tr} \mathbf{s}^2 \right)^{1/2} \tag{4b}$$

$$\theta = -\frac{1}{3} \sin^{-1} \left( \frac{3\sqrt{3} \det \mathbf{s}}{2J^3} \right) \tag{4c}$$

where $\mathbf{s}$ is the deviatoric stress tensor $\mathbf{s} = \boldsymbol{\sigma}' - p\mathbf{I}$.

The initial yield limit is denoted by using $\varphi_{ini}$ and $c_{ini}$ in Eq. (3) which are material parameters. In the same way, the failure limit is obtained by replacing $\varphi$ and $c$ by the peak values $\varphi_{peak}$ and $c_{peak}$. Non-linear isotropic hardening is considered, driven by the evolution of the yield parameters. The equivalent plastic strain has been chosen as the state variable controlling this evolution, defined as,

$$\varepsilon_{eq}^{p} = \left( \frac{2}{3} \boldsymbol{\varepsilon}^{p} : \boldsymbol{\varepsilon}^{p} \right)^{1/2} \tag{5}$$

where $\boldsymbol{\varepsilon}^{p}$ is the plastic strain tensor.

The friction angle varies in a piecewise manner as shown in Figure 1; the evolution laws corresponding to each zone are given in Table 2. Cohesion evolves in parallel with the friction angle according to:

$$c_{mob} = c_{peak} \cot\varphi_{ini} \tan\varphi_{mob} \tag{6}$$

where $c_{mob}$ is the mobilized cohesion, $c_{peak}$ is the peak cohesion, and $\varphi_{ini}$ and $\varphi_{mob}$ are the initial and mobilized friction angles, respectively.

It is well known that associated flow rules for geomaterials tend to overestimate volumetric strains during plastic flow. Therefore a non-associated flow rule is adopted in the model. Rather than deriving a specific function for the plastic potential, the flow rule is directly obtained from the yield/failure criterion in the following way,

$$\frac{\partial g}{\partial \boldsymbol{\sigma}'} = \omega \frac{\partial f}{\partial p}\frac{\partial p}{\partial \boldsymbol{\sigma}'} + \frac{\partial f}{\partial J}\frac{\partial J}{\partial \boldsymbol{\sigma}'} + \frac{\partial f}{\partial \theta}\frac{\partial \theta}{\partial \boldsymbol{\sigma}'} \tag{7}$$

where $g$ is the plastic potential and $\omega$ is a constant that controls the volumetric component of plastic deformations. With $\omega = 1$ an associated flow rule is recovered, while with $\omega = 0$ no volumetric plastic strains occur. An adequate value for geomaterials usually lies between these limits.

The model has been extended to consider cross-anisotropy through a non-uniform scaling of the stress tensor, as described in [23]. As Figure 2 shows, the local coordinate system 1-2-3 corresponds to the principal axes of anisotropy with direction “2” oriented orthogonal to the isotropic plane. In a general case, the global coordinate system, x-y-z, does not coincide with the local anisotropy one. Transformation of the stress tensor from global to local coordinates is achieved via the usual rotation transformation:

$$\boldsymbol{\sigma}'^{r} = \mathbf{a}\ \boldsymbol{\sigma}'\ \mathbf{a}^{T} \tag{8}$$

where $\boldsymbol{\sigma}'^{r}$ is the stress tensor orientated with the local coordinate system, and **a** is the rotation matrix:

$$\mathbf{a}=\begin{bmatrix} \cos\beta\cos\alpha & \sin\beta & -\cos\beta\sin\alpha \\ -\cos\alpha\sin\beta & \cos\beta & \sin\beta\sin\alpha \\ \sin\alpha & 0 & \cos\alpha \end{bmatrix} \tag{9}$$

where $\alpha$ and $\beta$ are the angles indicated in Figure 3.

The cross-anisotropic extension of the model is obtained by replacing $p'$ $J$ and $\theta$ in Eq. (3) by $p'^{ani}$ $J^{ani}$ and $\theta^{ani}$ respectively. These variables are invariants with the same definition as shown in Eq. (4) but calculated from the anisotropic stress tensor $\boldsymbol{\sigma}'^{ani}$. This tensor is obtained through the non-uniform scaling of the effective stress tensor oriented with the local coordinate system ($\boldsymbol{\sigma}'^{r}$), as shown below,

$$\boldsymbol{\sigma}'^{ani}=\begin{bmatrix} \dfrac{\sigma'^{r}_{11}}{c_N} & c_S\sigma^{r}_{12} & \sigma^{r}_{13} \\ c_S\sigma^{r}_{12} & c_N\sigma'^{r}_{22} & c_S\sigma^{r}_{23} \\ \sigma^{r}_{13} & c_S\sigma^{r}_{23} & \dfrac{\sigma'^{r}_{33}}{c_N} \end{bmatrix} \tag{10}$$

where $c_N$ and $c_S$ are the normal and shear scaling factors respectively.

An appropriate selection of strength parameters and scaling factors allows a satisfactory matching of a specified strength variation with loading orientation. Details about the physical meaning of the anisotropy parameters, their effects and of the derivation of the corresponding elastoplastic constitutive matrix are given in [23].

.

*2.2 Time-dependent mechanism*

For the time-dependent response, an additional mechanism is considered characterized by a modified form of Lemaitre's law. Assuming small strains, the total strain increment is decomposed as the sum of the two mechanisms,

$$d\boldsymbol{\varepsilon} = d\boldsymbol{\varepsilon}^{ep} + d\boldsymbol{\varepsilon}^{vp} = d\boldsymbol{\varepsilon}^{ep} + dt\left(\dot{\boldsymbol{\varepsilon}}^{vp}\right) \tag{11}$$

where $d\boldsymbol{\varepsilon}$ is the total strain increment; $d\boldsymbol{\varepsilon}^{ep}$ is the elastoplastic strain increment, related to the instantaneous response; $d\boldsymbol{\varepsilon}^{vp}$ is the viscoplastic strain increment, related to the time-dependent response; $dt$ is the time increment, and $\dot{\boldsymbol{\varepsilon}}^{vp}$ is the viscoplastic strain rate tensor. This strain decomposition gives rise to a class of constitutive relationship than can describe both elastoplastic properties and viscous behavior [24].

It is assumed that viscoplastic deformations are mainly caused by deviatoric stresses and the strain rates are given by:

$$\dot{\boldsymbol{\varepsilon}}^{vp} = \frac{2}{3}\frac{\dot{\varepsilon}^{vp}}{q}\mathbf{s} \tag{12a}$$

$$q = \left(\frac{3}{2}\mathbf{s}:\mathbf{s}\right)^{1/2} \tag{12b}$$

$$\dot{\varepsilon}^{vp} = \gamma\left\langle q - \sigma_s \right\rangle^n \left(1 - \varepsilon_{eq}^{vp}\right)^m \tag{12c}$$

where $\gamma$ is a viscosity parameter, $\sigma_s$ is a threshold from which viscoplastic strains are activated, $\langle\ \rangle$ are the Macaulay brackets, $n$ and $m$ are material constants, and $\varepsilon_{eq}^{vp}$ is the state variable of the time-dependent response given by,

$$\varepsilon_{eq}^{vp} = \int_o^t \left(\frac{2}{3}\dot{\boldsymbol{\varepsilon}}^{vp}:\dot{\boldsymbol{\varepsilon}}^{vp}\right)^{1/2} dt \tag{13}$$

In this way, larger viscoplastic strain rates are obtained for higher deviatoric stresses, and those rates decrease as viscoplastic strains accumulate in time, as observed in

laboratory tests. In the numerical implementation, an explicit scheme is employed, i.e. viscoplastic strains are computed from the stress state at the beginning of the step. These strains are subtracted from the total strain increment and the elastoplastic relationship is integrated only for $d\boldsymbol{\varepsilon}^{ep}$ using now an implicit scheme. This procedure allows preserving the standard format of the elastoplastic constitutive matrix, and it is considered accurate enough if small time steps are used.

*2.3 Unsaturation*

In case of unsaturation the retention curve linking suction and equivalent degree of saturation is given by the following modified Van Genuchten [25] expression:

$$S_e = \frac{S_l - S_{lr}}{S_{ls} - S_{lr}} = \left[ 1 + \left( \frac{s}{P} \right)^{\frac{1}{1-\lambda}} \right]^{-\lambda} \tag{14}$$

where $S_l$ is the degree of saturation, $S_{lr}$ is the residual degree of saturation, $S_{ls}$ is the degree of saturation in saturated conditions (normally 1), and $P$ and $\lambda$ are model parameters.

*2.4 Hydraulic*

Water flow is governed by Darcy's law using a hydraulic conductivity, **K**, given by

$$\mathbf{K} = \frac{\mathbf{k} k_r}{\mu_w} \tag{15}$$

where $\mathbf{k}$ is the intrinsic permeability tensor, $k_r$ is the relative permeability and $\mu_w$ is the water viscosity.

The relative permeability is considered a function of the effective degree of saturation, defined thought a generalized power law,

$$k_r = AS_e^{\Lambda} \tag{16}$$

where $A$ and $\Lambda$ are material parameters.

In the context of argillaceous materials, it is necessary to take into account the large increase of permeability that occurs when the rock experiences damage. In order to reproduce this phenomenon, permeability cannot be constant but should evolve with damage growth. In the context of the current elastoplastic model, this feature is incorporated by including a dependency of the intrinsic permeability on the plastic multiplier. An exponential function has been adopted for this purpose:

$$\mathbf{k} = \mathbf{k}_0 e^{\eta \lambda^p} \tag{17}$$

where $\mathbf{k}_0$ is the intrinsic permeability of the intact rock, $\eta$ is a constant that controls the rate of change and $\lambda^p$ is the cumulative value of the plastic multiplier.

## 3. Simulation of COx claystone mechanical behaviour

The constitutive model above has been applied to the reproduction of triaxial and creep tests performed on COx claystone samples. Parameters derived from this exercise are later applied to the analysis of an underground excavation. In all cases (triaxial and creep tests), the major principal stress was orthogonal to the bedding planes of the sample. Due to deconfinement and sample preparation, the specimens became unsaturated with an associated suction that corresponds to a relative humidity of 90%. This resulted in an increase of the sample strength which had to be taken into account in the simulation of the tests in order to obtain consistent effective parameters.

The initial suction of the sample has been computed with the psychrometric equation:

$$s = -\frac{RT}{M_w}\rho_l \ln(H_R) \tag{18}$$

where $R$ in the universal gas constant, $T$ is the temperature, $M_w$ is the water molar mass, $\rho_l$ is the density of the water and $H_R$ is the relative humidity. Assuming $R$=8.314 J/mol/K, $M_w$ = 0.019 kg/mol, $\rho_l$ = 1000 kg/m$^3$ and $T$=20ºC, a suction value of 14.26 MPa is obtained. It has been taken as the initial condition of the samples for the simulations.

Two triaxial tests under confinement pressures of 6 and 12 MPa respectively have been modelled. The tests were performed under displacement control with a constant strain rate of $10^{-6}$ s$^{-1}$ and conditions of null flux were applied to all boundaries. Figure 4 shows the stress-strain curves obtained from the simulated triaxial tests together with the laboratory test results. Figure 5 shows the results in terms of volumetric strains. From both figures a satisfactory agreement between the simulation results and the laboratory data can be noted. Table 3 summarizes the parameters of the mechanical and hydraulic constitutive model employed. Both tests share the same parameters except for $\xi_1$, $\xi_2$ and $\xi_3$ that show a dependency with confinement pressure that has not been taken into account in the model.

The simulated creep tests were also performed under triaxial loading conditions. In this case the controlled displacements were stopped once the desired deviatoric stress was reached, and, from then on, the stress state was kept constant for a specified period of time. Three test were performed at a confinement pressure of 12 MPa and with different ratios between applied and maximum deviatoric stresses (50, 75 and 90%). Figure 6 shows the results obtained in terms of time-dependent deformation. Somewhat larger differences compared with the results of the triaxial tests can be observed although the main trends of

behaviour are adequately captured. The parameters related the time-dependent response are also given in Table 3.

## 4. Theoretical formulation

To apply the constitutive model to a boundary value problem, it was incorporated into a general coupled hydromechanical formulation that is briefly described here. The formulation is a particular case of the general formulation presented in [26] for non-isothermal conditions. Only two phases are considered, solid ($s$) and liquid ($l$), corresponding to the two species mineral and water. In this case, the relevant balance equations are:

Balance of solid,

$$\frac{\partial}{\partial t}\left[\rho_s\left(1-\phi\right)\right]+\nabla\cdot\left(\mathbf{j}_s\right)=0 \tag{19}$$

Balance of water mass,

$$\frac{\partial}{\partial t}\left(\rho_l S_l \phi\right)+\nabla\cdot\left(\mathbf{j}_l\right)=f^w \tag{20}$$

Equilibrium,

$$\nabla\cdot\boldsymbol{\sigma}+\mathbf{b}=\mathbf{0} \tag{21}$$

where $\rho$ is the density, $\phi$ is the porosity, $\mathbf{j}$ is the total mass flux, $S_l$ is the liquid degree of saturation, $f^w$ is an external supply of water, $\boldsymbol{\sigma}$ is the stress tensor, $\mathbf{b}$ is the vector of body forces.

Using the definition of material derivative,

$$\frac{D_s\left(\bullet\right)}{Dt}=\frac{\partial\left(\bullet\right)}{\partial t}+\frac{d\mathbf{u}}{dt}\cdot\nabla\left(\bullet\right) \tag{22}$$

Eq. (19) becomes,

$$\frac{D_s\phi}{Dt} = \frac{1}{\rho_s}\left[(1-\phi)\frac{D_s\rho_s}{Dt}\right] + (1-\phi)\nabla\cdot\frac{d\mathbf{u}}{dt} \tag{23}$$

where **u** are displacements.

Now, the solid mass balance (Eq. 23) can be eliminated by introducing it into the water mass balance relationship (Eq. 20). Making use of the material derivative definition again, the following equation results,

$$\phi\frac{D_s(\rho_l S_l)}{Dt} + \rho_l S_l\frac{D_s\phi}{Dt} + (\rho_l S_l\phi)\nabla\cdot\frac{d\mathbf{u}}{dt} + \nabla(\mathbf{j}_l) = f^w \tag{24}$$

Any hydromechanical analysis involves the simultaneous solution of equations (21) and (24) together with appropriate constitutive models and equilibrium restrictions. Displacements and pore water pressure are the main unknowns to be determined.

## 5. Application to an underground excavation in COx claystone

### *5.1. GCS drift excavation*

The GCS drift was excavated at the -490 m level of the MHM URL in the location shown in Figure 7. The drift alignment was parallel to the major horizontal principal stress. As a result, the state of stress perpendicular to the axis of the tunnel was practically isotropic with $\sigma_v$ = 12.7 and $\sigma_h$ = 12.4 MPa. The *in situ* pore water pressure at that level in zones not affected by excavations is 4.7 MPa. The drift section is circular with a 2.6 m radius and was excavated with a road header. The advances of the excavation were generally 1.2 m long and were supported by an 18 cm thick fibre reinforced shotcrete shell and a number of 3 m long bolts in the crown area. 12 yielding concrete props were also installed. In addition, 12-m long rock bolts were also used in the front face. More details of the GCS

drift are given in [27], while a complete description of the excavation work has been presented in [28].

The excavation was monitored from instruments placed in boreholes drilled in advance from nearby openings. Displacements were measured by extensometers and inclinometers and pore water pressures by means of multipacker systems. In addition, convergences were also measured just after a particular section had been reached by the excavation advance. A more detailed account of the instrumentation and the monitoring observations is given in [20 this issue].

The damaged zone around the excavations has been the object of an intense site investigation [27]. As Figure 8 shows, the extent of the fractured zone is markedly larger in the horizontal direction compared to the vertical one in spite of the quasi-isotropic *in situ* stress state, indicating plainly the role played by the anisotropy of the material. Anisotropy is also evident in the measured convergences in different sections (Figure 9) with horizontal displacements significantly larger then vertical ones.

Another relevant observation for modelling concerns the permeability measured after excavation in boreholes drilled vertically and horizontally from the GCS drift [27]. As Figure 10 indicates, permeability increases sharply near the excavation and the extent of the zone of permeability increase is significantly larger in the horizontal direction, consistent with the observations of the damaged zone mentioned above.

### *5.2. Main features of the numerical model*

Many of the features of the analyses were specified in the “Action Transverse” benchmark [20 this issue] and correspond to a somewhat idealized simulation of the excavation process. They include the adoption of plane strain conditions and the assumption of no

gravity effects. Plane strain models are not able to fully reproduce the actual stress history and tend to underestimate deformations. Nevertheless, the differences with respect to a fully three-dimensional analysis tend to be small in the case of flexible supports with completion close to the face [30]. The mesh and main boundary conditions are illustrated in Figure 11 where the quasi-isotropic initial stress state can be noted. The initial horizontal stress perpendicular to the analysed cross-section is 16.1 MPa. Advantage has been taken of the symmetry of the problem to analyse only a quarter of the domain. Excavation is simulated through the deconfinement curve specified in [20 this issue] and shown in Figure 12. Deconfinement ratio is defined as the ratio between the surface stress applied to the boundary and the value in equilibrium with the initial stress condition. A negative distance to front indicates that the excavation front has not yet reached the analysis section. It can be observed that the stresses on the drift boundary reduce to 0.3 MPa, assumed to correspond to the soft support provided by shotcrete, rock bolts and yielding props. Figure 12 also shows the pore pressure applied to the boundary as a function of the nominal distance to the front. A Biot coefficient of 0.6 was adopted as specified in [20 this issue].

The parameters used in the simulation are basically those obtained from the calibration of the constitutive model listed in Table 3. Regarding the values $\xi_1$, $\xi_2$ and $\xi_3$ that showed a dependency with the confinement pressure, the values for the triaxial test with $\sigma_3 = 6$ MPa have been employed, since this confinement pressure represents an intermediate value between the *in situ* conditions and the maximum deconfinement occurring in the tunnel wall.

Rock strength anisotropy was defined by adopting scaling factors $c_N = 1.33$ and $c_S = 1.0$, selected to obtain a reasonable configuration of the damaged zone. The

stratification planes in the COx formation are nearly horizontal; therefore the angles $\alpha$ and $\beta$ (Figure 3) were set equal to zero. Regarding the elastic stiffness anisotropy, a ratio between the horizontal and vertical Young's modulus of 1.3 was employed, consistent with the values obtained from measurements of wave velocities in cubic samples [29].

In addition, it is necessary to specify the intrinsic permeability of the intact rock as well as the parameter controlling the variation of permeability with plastic multiplier, $\eta$ (Eq. (17)), see Table 4. The selected intrinsic permeability corresponds to the values of hydraulic conductivity measured *in situ* far away from the excavation damaged zone.

### *5.3. Results of the analysis*

The results from the numerical simulations are compared with field observations. Fig. 13 shows the location of the measurement points on the plane normal to the tunnel axis that have been used in the comparisons. They belong to three boreholes excavated from an adjacent drift (GAT); two devoted to the measurement of liquid pressure (OHZ1521, OHZ1522), and the other one to the measurement of rock displacements with an extensometer (OHZ1501). All of them were installed prior the excavation of the GCS drift. Also, a number of convergence sections installed along the drift during the excavation (OHZ170_24, OHZ170_36) are also considered.

Pore pressures are especially sensitive to the coupled hydromechanical rock behaviour. Figure 14 shows the evolution of the liquid pressure at the measurement points of borehole OHZ1521, together with the results of the analysis. It should be noted that the simulation times have been slightly shifted from point to point to take into account the fact that the borehole is not perfectly orthogonal to the tunnel axis. An adequate match between the

simulation results and the field data can be observed. Points PRE_02 and PRE_03 are quite close to the excavation and the liquid pressure drops very rapidly just after the front passes the corresponding cross section. Although this is partially explained by the decrease of the mean stress in this zone and the occurrence of dilatancy during plastic straining, the rate and the magnitude of this drop cannot be explained without considering the permeability increase due to the material damage. The model is also able to reproduce the liquid pressure increase in PRE_04 before the crossing of the excavation, although the observed maximum peak value was not quite reached. Even though the field data shows that this peak is maintained for some time, in the model the liquid pressure begins to fall just after the front passes but it should be remembered that the three dimensional effects of tunnel excavation are modelled here in a quite approximate manner. At point PRE_05, model results and field data show a very similar behaviour, although the field data starts from a somewhat lower value of liquid pressure.

Figure 15 shows the evolution of the liquid pressure at the measurement points OHZ1522 corresponding to both field data and simulation results (again the fact that the borehole is not exactly normal to the drift axis has been taken into account in the comparison). Here a good agreement is observed for points PRE_01 and PRE_05, but some departures are observed in the other locations. Field measurements points PRE_02, PRE_03 and PRE_04 exhibit a rapid drop of the liquid pressure after the excavation front passes its correspondent section, suggesting a permeability increase in those locations. Both field observations and the numerical model indicate that those points are not damaged, so the permeability was assumed constant and equal to the undamaged value during the entire simulation. The cause of this drop in the measured pore pressures deserves further study.

The horizontal displacements recorded by the extensometer in borehole OHZ1501 are shown in Figure 16, together with the result of the analysis. Again, the simulation times were shifted to match the time when the front was in the section of the measurement point. The extensometer is installed horizontally at the level of the axis of the drift, thus crossing the damaged zone at its maximum extent. The field data indicate that points DF0_02, DF0_03 and DF0_04 undergo relatively large displacements as they are within the damaged zone. In the simulation, points DF0_02 and DF0_03 show displacements of this order of magnitude and, in the case of DF0_02, with a very close quantitative agreement. Although point DF0_04 is within the plastic zone according to the simulation, computed displacements are smaller than the field observations; it seems that damage is underestimated at this location. The observed displacements at points further away than DF0_04 are quite small, both in the simulation and in the observations as expected for the undamaged zone of the rock.

The computed and observed convergences are shown in Figure 17. As convergence measurement points were installed just after the excavation front cleared the corresponding section, displacements that occur before the front reaches the analysis section were subtracted from the final results of the numerical model in order to achieve a proper comparison with field data. It can be observed that the computed horizontal convergences are quite close to the field observations and that they are, because of anisotropy, larger than the corresponding vertical ones. However the degree of anisotropy observed in the convergence field data is underestimated by the model. It is also worth noting that the rate of development of displacements with time appears to be well reproduced thus giving support to the adopted time-dependent model.

An estimate of the configuration of the damaged zone can be obtained by plotting contours of the cumulative plastic multiplier as it is directly related to the magnitude of irreversible strains (Figure 18). It can be seen that the configuration of the damaged zone is similar to that observed *in situ*, extending more in the horizontal direction (Figure 8). As the initial stress state is nearly isotropic, the use of an isotropic model would have resulted in an axisymmetric damage zone configuration; only an anisotropic model can account for the pattern of field observations.

Finally, the same analysis has been performed without considering creep deformations. Figure 19 shows the convergences obtained. When compared to Figure17, it can be observed that creep has a very small influence during the excavation stage; almost the same deformations are obtained. From this point on, the observed time dependency in Figure 19 is caused by consolidation only, but these deformations are quite small compared to the field measurements, demonstrating the importance of incorporating creep in the modelling of this type of materials.

## 6. Concluding remarks

This paper presents a constitutive model for argillaceous rocks, developed within the framework of elastoplasticity that includes a number of features that are relevant for a satisfactory description of their hydromechanical behaviour: anisotropy of strength and stiffness, behaviour nonlinearity and occurrence of plastic strains prior to peak strength, significant softening after peak, time-dependent creep deformations and permeability increase due to damage. Both saturated and unsaturated conditions are envisaged. The constitutive model has been successfully used in the simulation of triaxial and creep tests on COx claystone.

The constitutive model has then been applied, via a suitable coupled hydromechanical formulation, to the analysis of the excavation of a drift in the MHM URL, at a depth of 490 m. The pattern of observed pore water pressure and displacements, as well as the shape of the damaged zone, are generally satisfactorily reproduced although a number of departures of the calculations from field measurements have also been noted. Some of them may be related to the fact that an essentially 3D tunnel excavation problem has been simulated by a 2D analysis.

It has been shown that it is essential to incorporate material anisotropy if the field observations are to be adequately represented. Field observations also show the paramount importance of the development of the excavation damaged zone on the behaviour of the rock mass close to the drift. In the analyses presented, damage has been simulated in an approximate manner via a continuum approach whereas localisation and fractures are key characteristics of the damaged zone. Although the pattern of results has been largely recovered by the analyses performed, this continuum assumption can be considered the main limitation of the approach used in the calculations. Formulation and constitutive model are currently under development to simulate explicitly localisation and fracture phenomena in order to achieve a more realistic description of the damaged zone.

**Acknowledgements**

The financial and technical assistance of ANDRA to the work presented is gratefully acknowledged. The first author has been supported by a Conacyt scholarship (Reg. No. 270190).

**References**

[1] Gens A. The role of geotechnical engineering for nuclear energy utilisation. In: Vanicek I *et al.*, editors. Proc. 13th. European Conference on Soil Mechanics and Geotechnical Engineering, Prague: CGtS; 2004: 3, 25–67.

[2] Gens A. Environmental Geotechnics and Nuclear Waste. In: Datta M *et al.*, editors. Proc. of the 6th Int. Conference on Environmental Geotechnics. New Delhi: Tata McGraw Hill; 2010: 1, 64–75.

[3] Gens A. On the hydromechanical behaviour of argillaceous hard soils-weak rocks. In: Anagnostopoulos A *et al.*, editors. Proc. 15th European Conference on Soil Mechanics and Geotechnical Engineering – Geotechnics of Hard Soils – Weak Rocks (Part 4), Amsterdam: IOS Press; 2013: 71–118.

[4] Jardine RJ, Brosse A, Coop MR, Hosseini Kamal R. Shear strength and stiffness anisotropy of geologically aged stiff clays. In: Rinaldi VA *et al.*, editors. Deformation Characteristics of Geomaterials, Amsterdam: IOS Press; 2015: 156–191.

[5] Parry RHG. Some properties of a heavily overconsolidated Oxford clay at a site near Bedford. Géotechnique 1972; 22(3): 485–507.

[6] Wenk H-R, Voltolini M, Mazurek M, Van Loon LR, Vinsot A. Preferred orientations and anisotropy in shales: Callovo-Oxfordian shale (France) and Opalinus clay (Switzerland). Clays and Clays Minerals 2008; 56(3): 285–306.

[7] Vitone C, Cotecchia F, Desrues J, Viggiani G. An approach to the interpretation of the mechanical behaviour of intensely fissured clays. Soils and Foundations 2009; 49(3): 355–368.

[8] Kavvadas M, Amorosi A. A constitutive model for structured soils. Géotechnique 2000; 50(3):263–273.

[9] Rouainia M, Muir wood D. A kinematic hardening constitutive model for natural clays with loss of structure. Géotechnique 2000; 50(2):153–164.

[10] Liu MD, Carter JP. A structured Cam Clay model. Canadian Geotechnical Journal. 2002; 39:1313–1332 (2002).

[11] Gens A, Nova R., Conceptual bases for a constitutive model for bonded soils and weak rocks, In Anagnostopoulos A et al editors. Geotechnical Engineering of Hard Soils-Soft Rocks. Rotterdam: Balkema; 1993: 1, 485–494.

[12] Nova R, Castellanza R, Tamagnini C. A constitutive model for bonded geomaterials subject to mechanical and/or chemical degradation. International Journal for Numerical and Analytical Methods in Geomechanics 2003; 27:705–732.

[13] Suebsuk J, Horpibulsuk S, Liu MD. Modified structured cam clay: a generalised critical state model for destructured, naturally structured and artificially structured clays. Computers and Geotechnics 2010; 37:956–968.

[14] Souley M, Armand G, Su K, Ghoreychi M. Modeling the viscoplastic and damage behavior in deep argillaceous rocks. Physics and Chemistry of the Earth 2011; 36:1949–1959.

[15] Jia Y, Bian HB, Su K, Kondo D, Shao JF. Elastoplastic damage modeling of desaturation and resaturation in argillites. International Journal for Numerical and Analytical Methods in Geomechanics 2010; 34:187–220.

[16] Abou-Chakra Guéry A, Cormery F, Shao JF, Kondo D. A micromechanical model of elastoplastic and damage behavior of a cohesive geomaterial. International Journal of Solids and Structures 2008; 45(5):1406–1429.

[17] Huang Y, Shen WQ, Shao JF, Abou-Chakra Guéry A, Jia Y. Multi-scale modeling of time-dependent behavior of claystones with a viscoplastic compressible porous matrix. Mechanics of Materials 2014; 79:25–34.

[18] Delay J, Vinsot A, Krieguer JM, Rebours H, Armand G. Making of the underground scientific experimental programme at the Meuse/Haute-Marne underground research laboratory, North Eastern France, Physics and Chemistry of the Earth 2007; 32**:** 2–18.

[19] Armand G, Conil N, Talandier J, Seyedi D. Fundamental aspects of the hydromechanical behavior of the Callovo-Oxfordian claystone – from experimental investigations toward a modelling perspective. Computers and Geotechnics 2016; this issue.

[20] Seyedi D, Armand G, Noiret A.“Transverse Action”. A model benchmark exercise for numerical analysis of the Callovo-Oxfordian claystone hydromechanical response to excavation operations. Computers and Geotechnics 2016; this issue.

[21] Lemaitre J. A continuous damage mechanics model for ductile fracture. Journal of Engineering Materials and Technology 1985; 107(1): 83–89.

[22] Sloan SW, Booker JR. Removal of singularities in Tresca and Mohr-Coulomb yield functions. Communications in Applied Numerical Methods 1986; 2(2):173-179.

[23] Manica M, Gens A, Vaunat J, Ruiz DF. A cross-anisotropic formulation for elasto-plastic models. Geotechnique Letters 2016; 6: 156–162.

[24] Darve F. The expression of rheological laws in incremental form and the main classes of constitutive equations. In: Darve F editor. Geomaterials: Constitutive equations and modelling, Amsterdam: Elsevier; 1990: 123–148.

[25] Van Genuchten MT. A closed-form equation for predicting the hydraulic conductivity of unsaturated soils. Soil Science Society of America Journal 1980; 44(5):892–898.

[26] Olivella S, Carrera J, Gens A, Alonso EE. Non-isothermal Multiphase Flow of Brine and Gas through Saline media. Transport in porous media 1994; 15: 271–293

[27] Armand G, Leveau F, Nussbaum C, de La Vaissiere R, Noiret A, Jaeggi D, Landrein P, Righini C. Geometry and properties of the excavation-induced fractures at the Meuse/Haute-Marne URL drifts. Rock Mechanics and Rock Engineering 2014; 47:21–41.

[28] Bonnet-Eymard T, Ceccaldi F, Richard L. Extension of the Andra underground laboratory: methods and equipment used for dry, dust-free works. Proc. World Tunnel Congress, Helsinki; 2011.

[29] Armand G, Noiret A, Zghondi J, Seyedi DM. Short- and long-term behaviors of drifts in the Callovo-Oxfordian claystone at the Meuse/Haute-Marne Underground Research Laboratory. Journal of Rock Mechanics and Geotechnical Engineering 2013; 5:221–230.

[30] Cantieni L, Anagnostou G. The effect of the stress path on squeezing behaviour in tunnelling. Rock Mechanics and Rock Engineering 2009; 42(2): 289–318.

**Captions**

Figure 1. Friction angle evolution in hardening and softening regimes.

Figure 2. (a) Global and (b) local coordinate systems.

Figure 3. Definition of the angles in the rotation matrix [23].

Figure 4. Stress-strain curves in triaxial tests on COx claystone. Observations [19 this issue] and constitutive model results.

Figure 5. Volume change in triaxial tests on COx claystone. Observations [19 this issue] and constitutive model results.

Figure 6. Creep tests on COx claystone. Observations [19 this issue] and constitutive model results.

Figure 7. Location of the GCS drift in a three-dimensional view of the MHM URL [20 this issue].

Figure 8. Extension of the damaged zone for drifts parallel to the major horizontal stress [27].

Figure 9. Horizontal and vertical convergences in a drift parallel to the major horizontal stress [29].

Figure 10. Variation of in situ measured hydraulic conductivity with distance to the drift wall [27]. a) Vertical borehole b) Horizontal borehole.

Figure 11. Finite element mesh and boundary conditions.

Figure 12. Variation of boundary conditions on the excavation wall.

Figure 13. Location of measurement points used for comparison with simulation results.

Figure 14. Pore pressure evolution in measurement points of borehole OHZ1521. Observed [20 this issue] and computed values.

Figure 15. Pore pressure evolution in measurement points of borehole OHZ1522. Observed [20 this issue] and computed values.

Figure 16. Horizontal displacements at measurement points of borehole OHZ1501. Observed [20 this issue] and computed values.

Figure 17. Evolution of horizontal and vertical convergences. Observed and computed values.

Figure 18. Contours of accumulated plastic multiplier at the end of the excavation.

Figure 19. Evolution of horizontal and vertical convergences. Observed and computed values. No creep deformations considered.

**Tables**

Table 1. Reference properties of the COx claystone (modified from [3])

| | |
|---|---|
| Dry density (g/cm$^3$) | 2.21 - 2.33 |
| Porosity (%) | 11 – 16 |
| Water content (%) | < 6.5 |
| Liquid limit (%) | 21 – 25 |
| Plastic index (%) | 11 – 19 |
| Geological stage<br>(millions of years) | Callovo – Oxfordian<br>156 – 164 |

Table 2. Evolution laws for the mobilized friction angle (see Figure 1 for the location of the strain zones)

| | |
|---|---|
| Zone 1 | $\varphi_{mob} = \varphi_{ini} + \dfrac{\varepsilon_{eq}^{p}}{a_{hard} + \dfrac{\varepsilon_{eq}^{p}}{\Delta\varphi_{hard}}}, \quad \Delta\varphi_{hard} = \dfrac{\xi_1}{\dfrac{\xi_1}{\varphi_{peak} - \varphi_{ini}} - a_{hard}}$ |
| Zone 2 | $\varphi_{mob} = \varphi_{peak}$ |
| Zone 3 | $\varphi_{mob} = \varphi_{peak} - \dfrac{\varepsilon_{eq}^{p} - \xi_2}{a_{soft} + \dfrac{\varepsilon_{eq}^{p} - \xi_2}{\Delta\varphi_{soft}}}, \quad \Delta\varphi_{soft} = \dfrac{\xi_3 - \xi_2}{\dfrac{\xi_3 - \xi_2}{\varphi_{peak} - \varphi_{res}} - a_{soft}}$ |
| Zone 4 | $\varphi_{mob} = \varphi_{res}$ |

$\varphi_{mov}$ = mobilized friction angle, $\varphi_{res}$ = residual friction angle, $\xi_1$ = equivalent plastic strain at which the maximum strength is reached, $\xi_2$ = equivalent plastic strain at which softening begins, $\xi_3$ = equivalent plastic strain at which the residual strength is reached, $a_{hard}$ = constant that controls the curvature of the function in the hardening branch, $a_{soft}$ = constant that controls the curvature of the function in the softening branch.

Table 3. Constitutive law parameters used in the simulations

| Parameter | Units | Input value | Parameter | Units | Input value |
|---|---|---|---|---|---|
| *Instantaneous mechanism* | | | *Instantaneous mechanism (continuation)* | | |
| $E$ | (MPa) | 4000 | $\xi_3$ (6 MPa) | (-) | 0·021 |
| $\nu$ | (-) | 0·2 | $\xi_3$ (12 MPa) | | 0·06 |
| $\varphi_{peak}$ | (º) | 22 | *Time-dependent mechanism* | | |
| $\varphi_{ini}$ | (º) | 9·35 | $\sigma_s$ | (MPa) | 4 |
| $\varphi_{res}$ | (º) | 14·74 | $\gamma$ | (day$^{-1}$) | 1 x 10$^{-7}$ |
| $c_{peak}$ | (MPa) | 3·5 | $n$ | (-) | 3·37 |
| $a_{hard}$ | (-) | 0·0035 | $m$ | (-) | 530 |
| $a_{soft}$ | (-) | 0·07 | *Hydraulic* | | |
| $\omega$ | (-) | 0·6 | $k_{xx}$, $k_{yy}$, $k_{zz}$ | ( m$^2$) | 5 x 10$^{-20}$ |
| $\xi_1$ (6 MPa) | (-) | 0·005 | $A$ | (-) | 1 |
| $\xi_1$ (12 MPa) | | 0·012 | $\Lambda$ | (-) | 3 |
| $\xi_2$ (6 MPa) | (-) | 0·006 | $P$ | (MPa) | 14·3 |
| $\xi_2$ (12 MPa) | | 0·0165 | $\lambda$ | (-) | 0·33 |

Table 4. Hydraulic parameters used in the drift excavation simulation

| Parameter | Units | Input value |
|---|---|---|
| $k_{0xx}$, $k_{0yy}$, $k_{0zz}$ | (m$^2$) | 5 x 10$^{-20}$ |
| $B$ | (-) | 0·6 |
| $\eta$ | (-) | 300 |

**Figures**

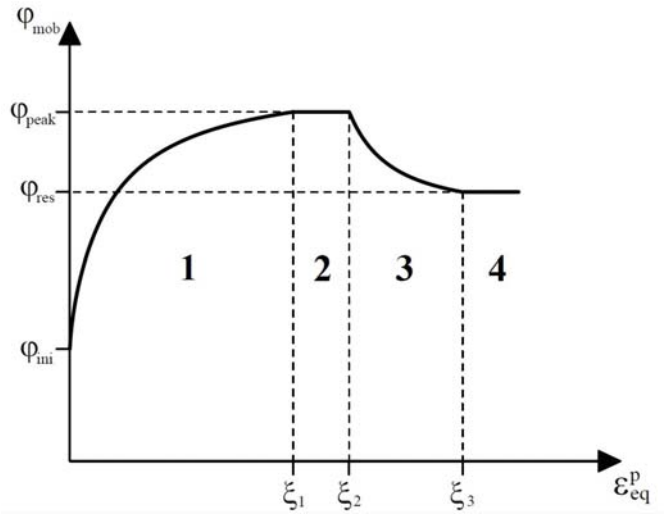


Figure 1. Friction angle evolution in hardening and softening regimes

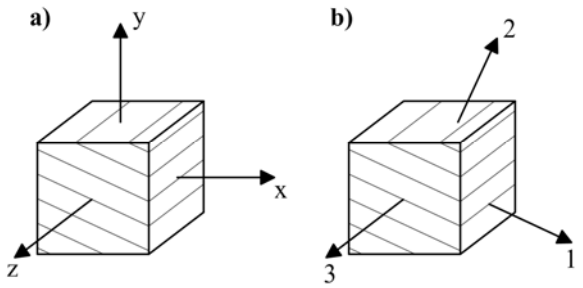


Figure 2. (a) Global and (b) local coordinate systems

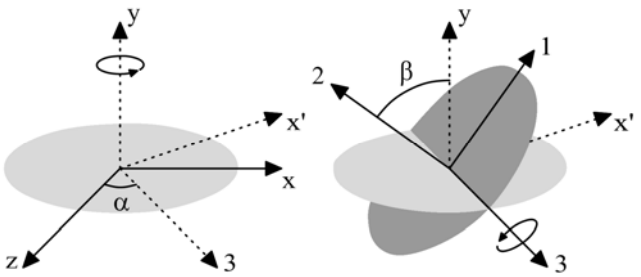


Figure 3. Definition of the angles in the rotation matrix [23]

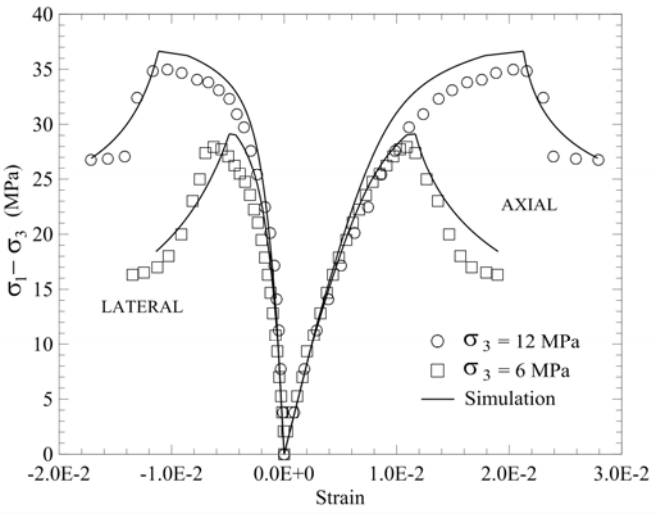


Figure 4. Stress-strain curves in triaxial tests on COx claystone. Observations [19 this issue] and constitutive model results

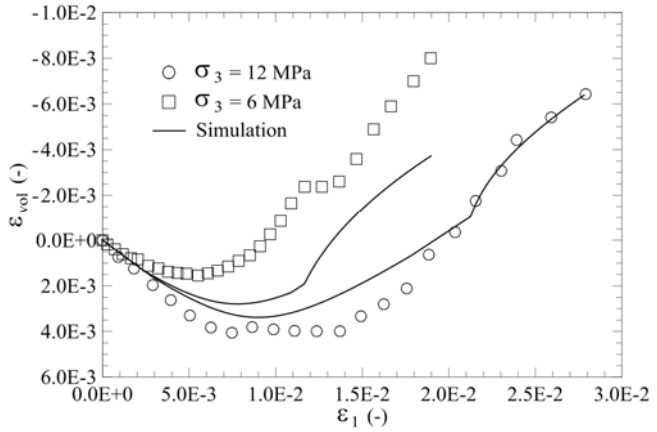


Figure 5. Volume change in triaxial tests on COx claystone. Observations [19 this issue] and constitutive model results

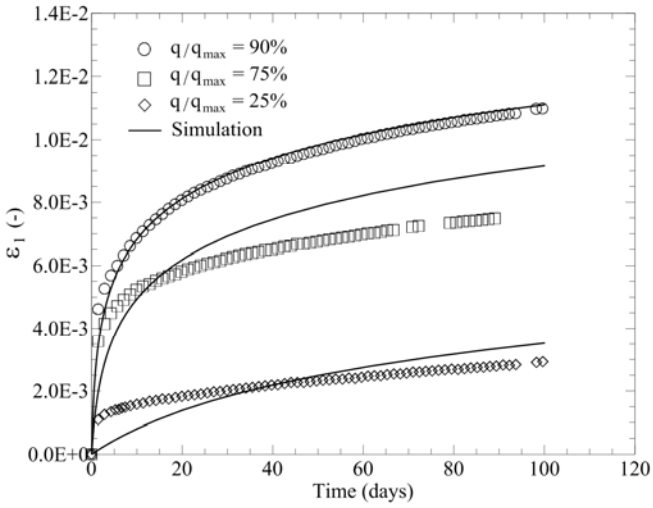


Figure 6. Creep tests on COx claystone. Observations [19 this issue] and constitutive model results

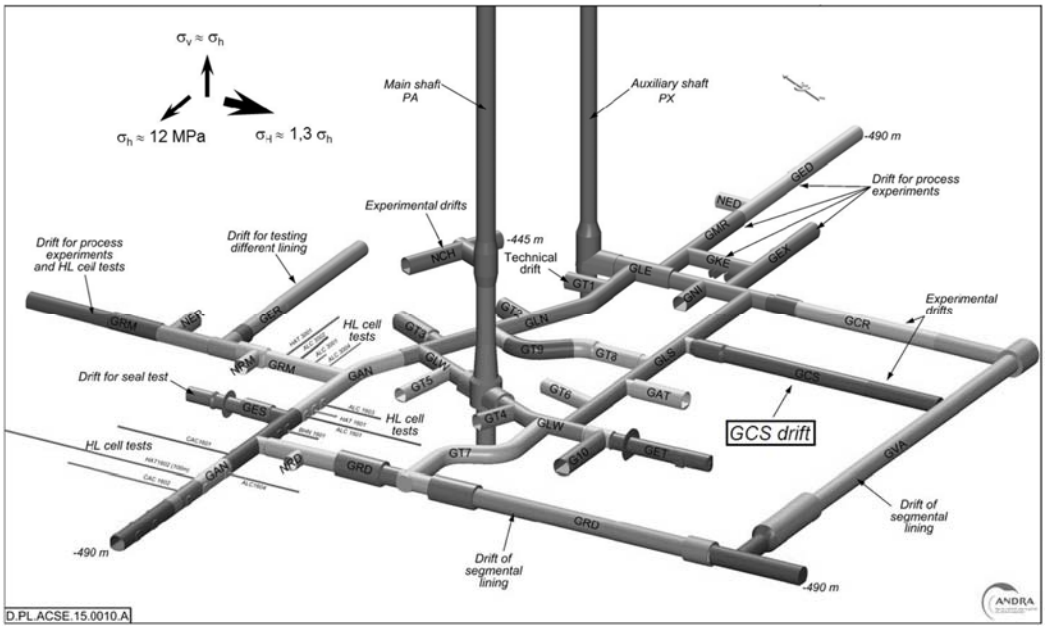


Figure 7. Location of the GCS drift in a three-dimensional view of the MHM URL [20 this issue]

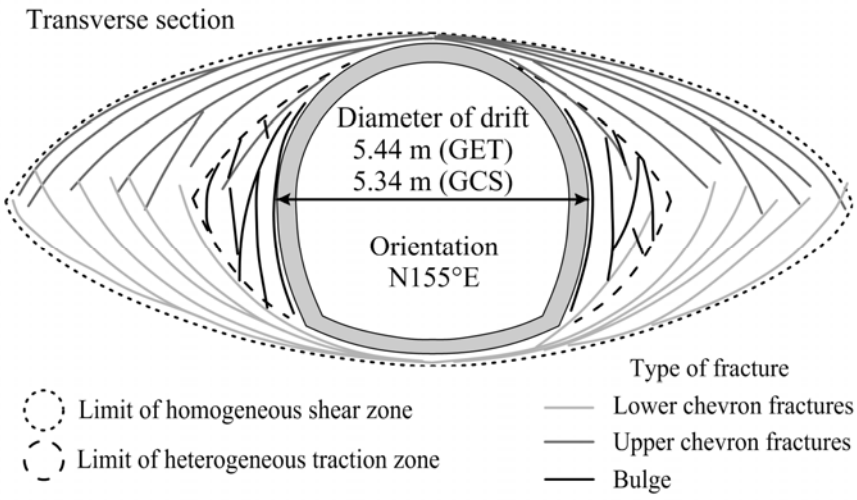


Figure 8. Extension of the damaged zone for drifts parallel to the major horizontal stress [27]

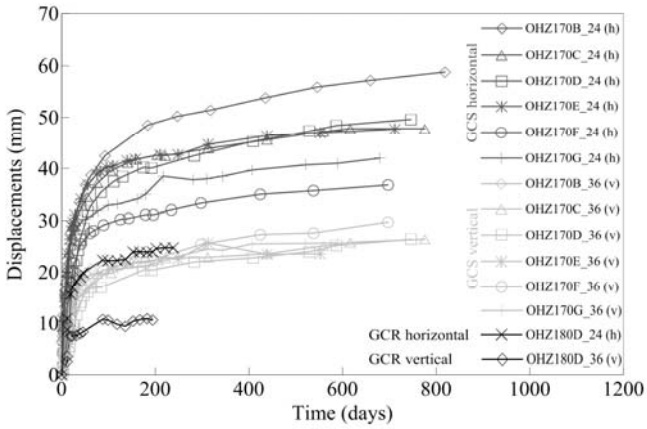


Figure 9. Horizontal and vertical convergences in a drift parallel to the major horizontal stress [29]

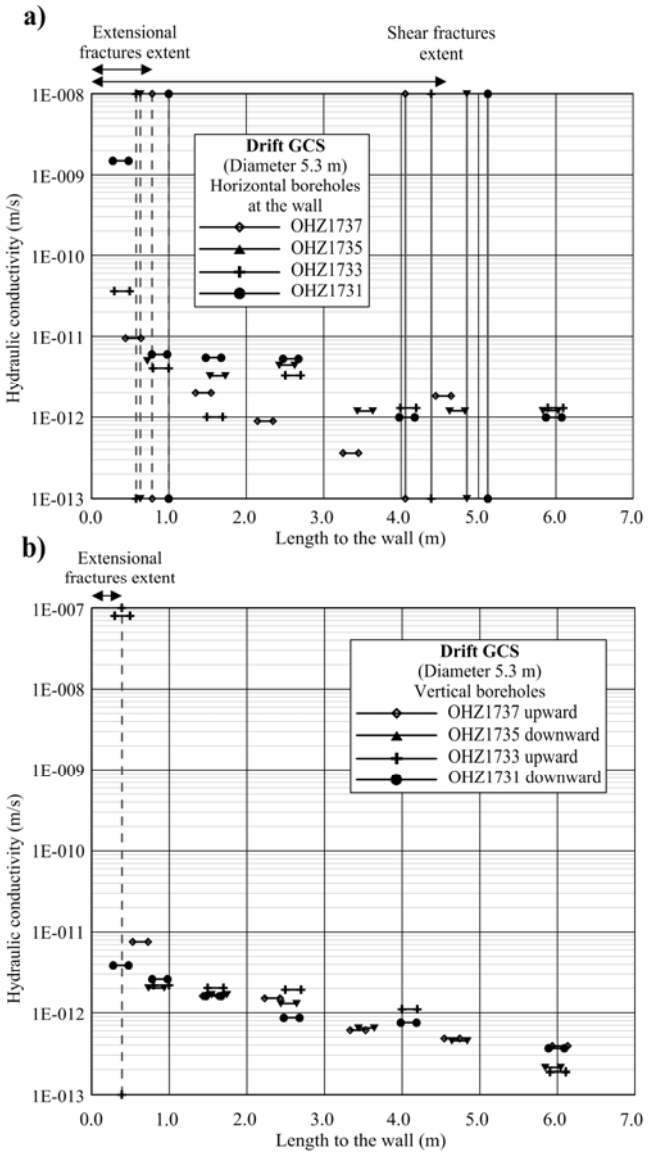


Figure 10. Variation of *in situ* measured hydraulic conductivity with distance to the drift wall [27]. a) Vertical borehole b) Horizontal borehole

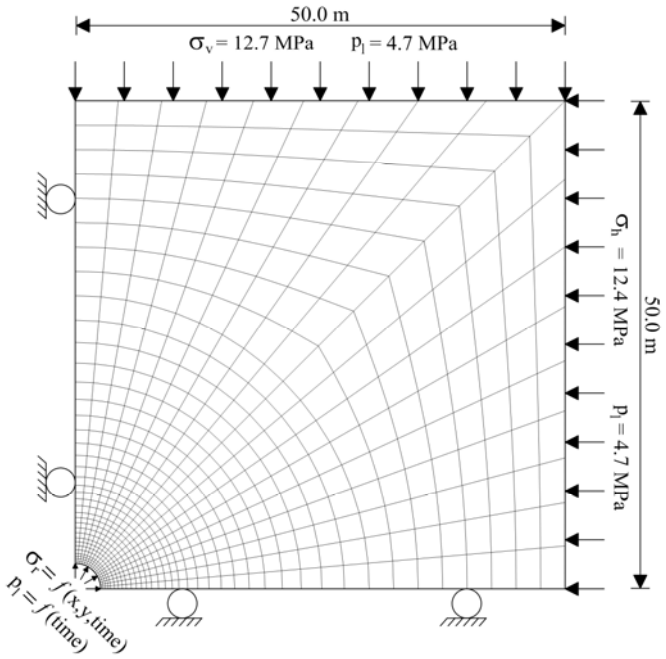


Figure 11. Finite element mesh and boundary conditions

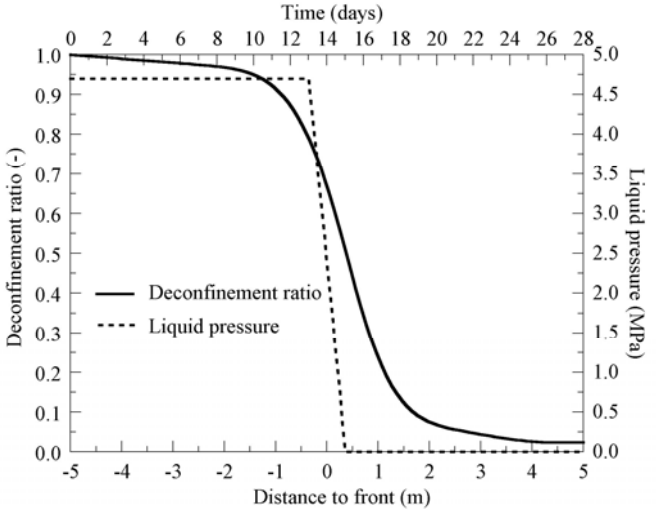


Figure 12. Variation of boundary conditions on the excavation wall

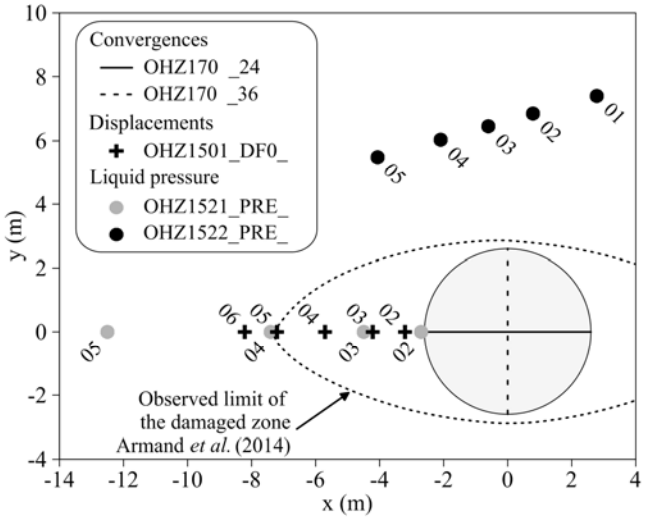


Figure 13. Location of measurement points used for comparison with simulation results

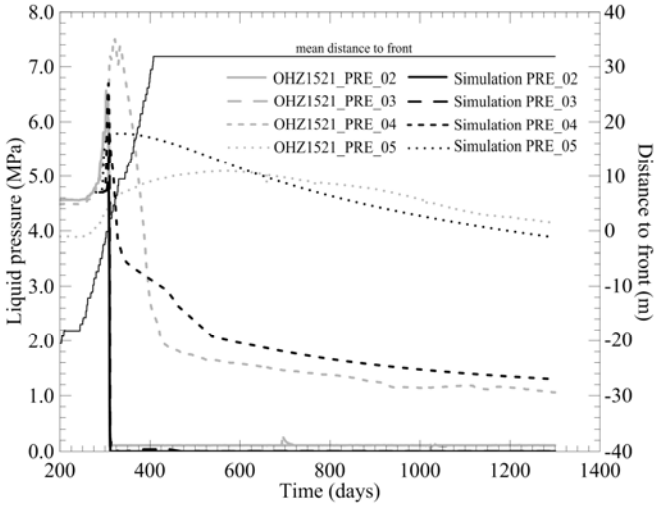


Figure 14. Pore pressure evolution in measurement points of borehole OHZ1521. Observed [20 this issue] and computed values

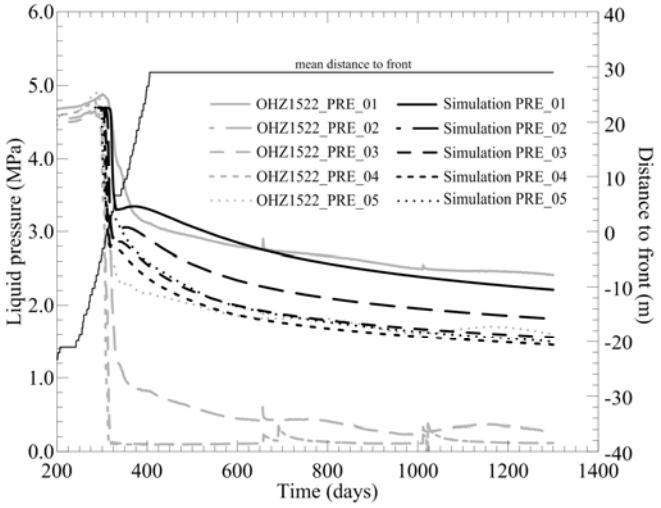


Figure 15. Pore pressure evolution in measurement points of borehole OHZ1522. Observed [20 this issue] and computed values

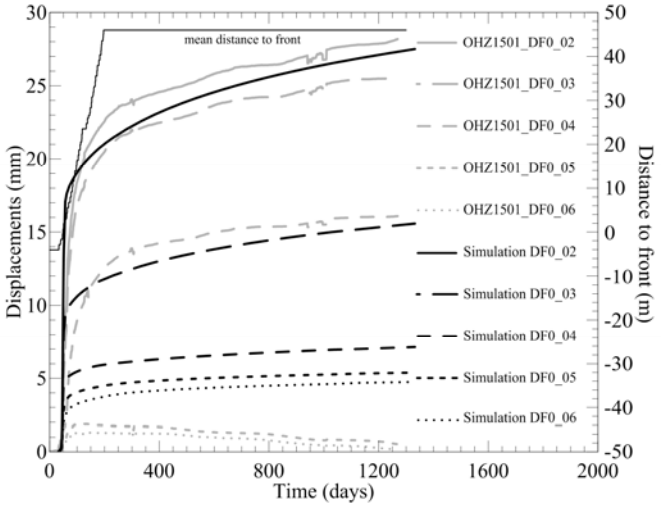


Figure 16. Horizontal displacements at measurement points of borehole OHZ1501. Observed [20 this issue] and computed values

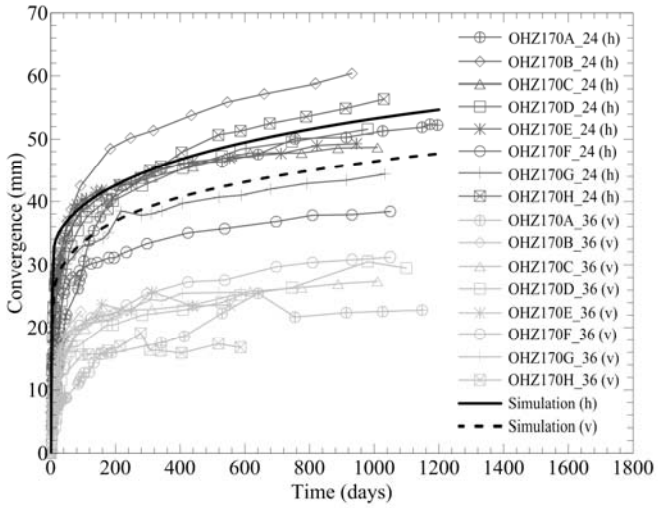


Figure 17. Evolution of horizontal and vertical convergences. Observed and computed values

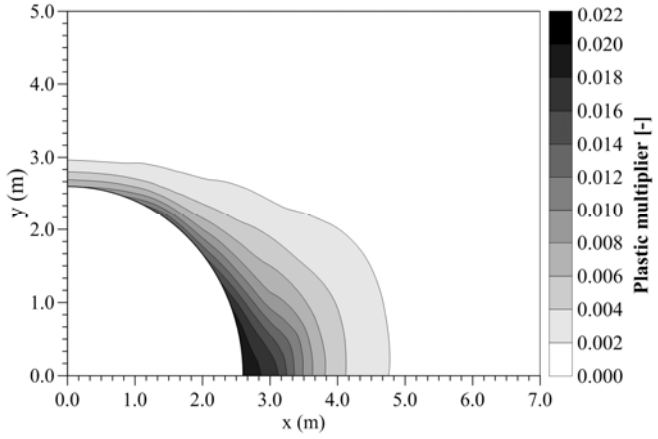


Figure 18. Contours of accumulated plastic multiplier at the end of the excavation

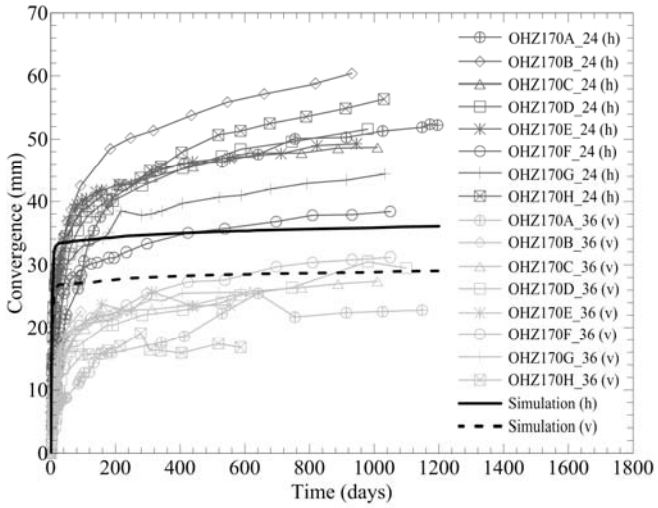


Figure 19. Evolution of horizontal and vertical convergences. Observed and computed values. No creep deformations considered